ROYAL SOCIETY OF CHEMISTRY

PAPER

Check for updates

Constructing a covalently Si–O–C bonded diatomite-derived SiO₂@C anode for high-capacity lithium-ion batteries

Qiaofu Zheng,[a] Licheng Wei,*[b] Lifeng Zhou,[a] Guannan Peng,[a] Dalei Sun*[a] and Yimin Chao [iD] *[b]

Silica-based materials, serving as one type of prospective electrode for advanced high-energy density LIBs (lithium-ion batteries), are encountering critical obstacles in commercialization, including inherently poor conductivity, volume expansion and particle pulverization. Herein, a ball-milled diatomite combined with glucose-derived carbon (DTm@GC) has been synthesized as an anode for LIBs by constructing a dense carbon network on the diatomite-derived SiO₂ through Si–O–C covalent bonding. The strong and dense Si–O–C covalent bond between the carbon network and diatomite accelerates migration of Li$^+$ and alleviates volume variation during lithiation/de-lithiation. The results show that the DTm@GC anode delivers a superior discharge specific capacity of 781 mA h g^{-1} after 100 cycles at 0.1 A g^{-1}, along with approximately 100% capacity retention. Furthermore, the synthesized anode can maintain a stable specific capacity of 613.79 mA h g^{-1} after 200 cycles at 0.5 A g^{-1}, and 456.68 mA h g^{-1} over 1000 consecutive cycles at 1 A g^{-1}. The outstanding electrochemical performance of DTm@GC with a strong covalent Si–O–C bond provides a valuable avenue for fabricating low-cost, high-performance SiO₂-based anodes for high-capacity LIBs.

Sustainability spotlight

Against the backdrop of a global paradigm shift toward sustainable energy storage architectures, driving the iterative upgrading of high-energy-density, eco-friendly lithium-ion batteries (LIBs) has become a key research priority in the energy sector. By utilizing natural diatomite as the feedstock, this work establishes a green fabrication process for SiO₂ anode materials that conforms to green chemistry principles, while demonstrating excellent scalability and low energy consumption. Experimental results confirm that the resultant anode exhibits a lithium-storage capacity far surpassing that of commercial graphite, as well as remarkable cycling stability and structural integrity. This work provides a robust impetus for engineering high-performance LIBs through sustainable manufacturing routes.

Introduction

It is widely acknowledged that lithium-ion batteries (LIBs) have established themselves as a core category of advanced technologies for electric vehicles and portable devices, due to their high energy density, long service life, and comparatively low price.[1–4] LIBs are composed of a cathode, anode, separator and electrolyte, of which the anode determines the overall capacity of the batteries. At present, LIBs assembled with commercial graphite electrodes, which have a theoretical specific capacity of 372 mA h g^{-1}, can hardly meet the requirements for long-life electric vehicles and industrial-scale energy storage devices.[5,6]

Compared to graphite, silicon (Si) exhibits a superior theoretical specific capacity (4200 mA h g^{-1}) and suitable operating potential (~0.4 V *vs.* Li$^+$/Li), which renders it a prominent prospective material for LIBs.[7–9] Unfortunately, the reaction between Si and Li$^+$ ions triggers a large volume expansion (>300%), leading to particle pulverization, repeated cracking, and continuous growth of the solid electrolyte interphase (SEI). Such structural and interfacial degradation ultimately results in a rapid decline in cell performance.[10,11] Compared to Si, silicon dioxide (SiO₂) exhibits more promising electrochemical prospects with medium theoretical specific capacity (~1965 mA h g^{-1}), moderate volume variation (~100%), and durable cycling stability.[12,13] During the initial discharge process, SiO₂ reacts with Li$^+$, generating Li₂O, lithium silicates and a Li$_x$Si alloy. The formation of Li₂O and lithium silicates is beneficial for constructing a stable SEI layer and accelerating the diffusion of Li$^+$, respectively.[14,15] However, a large quantity of Li$^+$ can be consumed during the generation of lithium silicates

[a]School of Chemical Engineering & Light Industry, Guangdong University of Technology, Guangzhou 510006, P. R. China. E-mail: zhengqiaofu1@mails.gdut.edu.cn; zhoulifeng@mails.gdut.edu.cn; pengguannan@mails.gdut.edu.cn; sdlei80@163.com

[b]Foshan Xianhu Laboratory, Foshan 430070, P. R. China. E-mail: weilicheng@xhlab.cn

and Li_2O, which gives rise to irreversible capacity depletion and impaired initial coulombic efficiency (ICE). Moreover, the considerable volume strain and low electrical conductivity of SiO_2 may reduce its electrochemical activity and specific capacity.[16,17]

To date, researchers have adopted a variety of strategies to modify the properties of SiO_2 materials to enhance their electrochemical performance in LIBs, such as regulating the crystal phase, constructing a hollow structure, and incorporating with conductive materials.[18,19] Among these strategies, constructing hollow porous structures is an effective method to alleviate volume strain and shorten the Li^+ diffusion path.[20,21] For example, Ma et al.[22] synthesized hierarchically porous multishell SiO_2 microspheres for LIB anodes, enabling a cell capacity of 750 mA h g^{-1} over 500 charge–discharge cycles. This result has confirmed that the porous hollow structure can reduce volume expansion and promote Li^+ migration, enhancing the electrochemical activity of silica and improving the capacity of LIBs. Aiming at the poor electrical conductivity of silica, an effective approach is to combine SiO_2 with highly conductive constituents, including carbon or metal oxides.[23,24] For instance, $SiO_2@TiO_2/rGO$ anodes are fabricated via wrapping graphene on $SiO_2@TiO_2$ core–shell microspheres, and they retain a specific capacity of 405.71 mA h g^{-1} following 1500 cycles at 1 A g^{-1} and a rate of capacity degradation below 20%.[25] Similarly, $SiO_2@C$ hollow spheres with 67 wt% SiO_2 are fabricated as anodes of LIBs, and they display a capacity performance of 649.6 mA h g^{-1} over 160 cycles.[26] However, these synthesis routes are reliant on toxic, flammable, and expensive chemical silicon sources, such as tetraethyl orthosilicate (TEOS), limiting their large-scale applications.

In contrast, diatomite (DT), featuring cost-effectiveness, eco-friendliness, and large-scale readiness, exhibits promising potential as a SiO_2-based anode for LIBs, owing to its unique inherent 3D hierarchical porous structure. Herein, we have prepared a composite of diatomite coupled with conductive carbon materials (DTm@GC) via an interface engineering strategy constructing a continuous carbon network with Si–O–C covalent bonds. This chemically bonded interface is conducive to enhancing charge transfer and confining volume strain, effectively modifying the poor conductivity and structural instability of silica. Therefore, the optimized DTm@GC anode has delivered outstanding electrochemical performances and cycling stability. This study has set the stage for developing high-performance, low-cost SiO_2-based anode materials by modifying the interface structure of SiO_2 for carriers.

Experimental

Materials preparation

Diatomite was obtained from Tianjin Damao Chemical Reagent Co., Ltd. Analytical grade hydrochloric acid (HCl) and glucose monohydrate ($C_6H_{12}O_6 \cdot H_2O$, 99%) were provided by Guangzhou Chemical Reagent Factory. Ethanol (C_2H_5OH, 99%) was supplied by Shanghai Macklin Biochemical Co., Ltd. Conductive carbon black (Super C65), polyacrylic acid (PAA) binder, copper foil, and electrolyte KLD-LP03 (1.0 M lithium

hexafluorophosphate ($LiPF_6$) dispersed in a mixture of ethylene carbonate (EC), dimethyl carbonate (DMC), and diethyl carbonate (DEC) (1:1:1, v/v/v) with 5 wt% fluoroethylene carbonate (FEC) as an additive) were obtained from Canrd Technology Co., Ltd. $LiFePO_4$ (LFP), conductive carbon black (Super P), polyvinylidene fluoride (PVDF), aluminum foil and N methyl 2 pyrrolidone (NMP) were procured from Shenzhen Kejing Star Technology Co., Ltd. The light-emitting diode (LED) was purchased from Alibaba Corporation. No additional purification was performed on the reagents prior to their application.

The diatomite was first calcined in air at 600 °C for 3 h to remove organic impurities. The resulting product was added into 1 M HCl (1:5 volume ratio) and stirred for 6 h to dissolve metallic impurities. The purified diatomite powder mixed with two sizes of zirconium dioxide (Zr_2O_3) balls (3 mm and 1 mm) and ethanol in a mass ratio of 5:1:2 was poured into a 50 mL ball-milled Zr_2O_3 jar and milled at 500 rpm for 24 h. The ball-milled diatomite was marked as DTm. The DTm powder was added into a mixture solution with 30 mL of H_2O and 3 g of $C_6H_{12}O_6 \cdot H_2O$, and transferred into a 50 mL polytetrafluoroethylene reactor. After ultrasonic mixing for 30 min, the reactor was sealed into a stainless-steel autoclave and reacted at 180 °C for 5 h. The yellowish-brown intermediate precipitate was washed with water and separated upon centrifugation (denoted as hydrothermal carbon mixed with diatomite (HTC/DTm)). This intermediate was annealed at 650 °C for 4 h in Ar at 5 °C min^{-1}, producing the final black powder of DTm@GC. A series of DTm@GC materials with different carbon contents were synthesized by changing the content of $C_6H_{12}O_6 \cdot H_2O$ to 2 g and 6 g, labeled as DTm@GC-2 and DTm@GC-6, respectively. In addition, the pure HTC intermediate was synthesized by hydrothermally reducing 3 g of $C_6H_{12}O_6 \cdot H_2O$ to elucidate the role of the hydrothermal carbon. Then, the pure hydrothermal carbon (HTC) intermediate was physically mixed with DTm powder and calcined under the same conditions to prepare the reference sample of DTm/GC.

Materials characterization

X-ray diffraction (XRD, Bruker D 8 Advance) was employed to obtain crystal information on the powder materials, with data collected over a 2θ range of 15–80°. A micro-fourier transform infrared spectrometer (micro-FTIR) was utilized to confirm the structural features of the composites. A LabRAM Odyssey laser confocal micro-Raman spectrometer (532 nm excitation) was used to characterize the chemical bonds and molecular vibration modes in the material. Thermogravimetric analysis (TGA) was performed on a METTLER-TOLEDO TGA/DSC1 instrument to analyse the mass variation of the materials. Nitrogen adsorption–desorption isotherms, combined with the BET (Brunauer–Emmett–Teller) method and BJH (Barrett–Joyner–Halenda) model, were employed to characterize the specific surface area, pore volume, and porous size of composites using a Micromeritics Tristar II-3020 system. Field emission scanning electron microscopy (FE-SEM) was carried out on a Zeiss GeminiSEM 500 microscope, disclosing the morphology of the

materials. The fine crystal information on the materials was analysed using a JEM-F200 transmission electron microscope (TEM) equipped with an energy dispersive spectroscopy (EDS) system. X-ray photoelectron spectroscopy (XPS) measurements were performed using a Thermo Scientific Escalab 250 Xi spectrometer under Al-Kα X-ray excitation to determine the chemical valence of the materials.

Electrochemical measurements

To prepare anode plates, a homogeneous slurry was obtained by blending 70 wt% DTm@GC, 20 wt% Super C65, and 10 wt% polyacrylic acid (PAA) binder, supplemented with a suitable volume of deionized water. This homogeneous slurry was deposited onto a copper foil to prepare an electrode, and dried in a vacuum oven at 80 °C for 16 h. The dry copper foil coated with the electrode material was cut into 10 mm diameter electrodes, where the areal loading of DTm@GC ranges from 1.2–1.5 mg cm^{-2}. LIB half-cells (CR2032 coin cells) were fabricated using DTm@GC as the working electrode, lithium foil as the counter electrode, Celgard 2400 as the separator, and KLD-LP03 as the electrolyte. Galvanostatic charge–discharge tests were carried out on a NEWARE battery testing system, with the voltage ranging from 0.01 and 3.0 V (vs. Li$^+$/Li) and current density increasing from 0.05 to 2 A g^{-1}. To fabricate the LFP cathode, an electrode slurry was obtained by blending the LFP, Super P conductive additive, and PVDF binder (in a mass ratio

of 8 : 1 : 1) and homogeneously mixing with NMP solvent. This slurry was subsequently spread on an aluminium foil and subjected to vacuum oven drying at 80 °C for 16 h. Prior to full-cell assembly, the DTm@GC anode underwent pre-lithiation in a half-cell using a lithium foil as the counter electrode, followed by activation via five cycles at 50 mA g^{-1}. The DTm@GC//LFP full cells were constructed with a pre-lithiated DTm@GC anode and LFP cathode, where the capacity ratio of anode/cathode was kept within 1.1–1.2. All cells were kept in an Ar-atmosphere glovebox with H$_2$O/O$_2$ content below 0.1 ppm. Cycling tests were performed at 0.1 C (1 C = 170 mA h g^{-1} based on LFP) within a voltage window of 2.5 to 3.8 V (vs. Li$^+$/Li). Cyclic voltammetry (CV) was conducted on an Ivium OctoStat200 electrochemical workstation, while electrochemical impedance spectroscopy (EIS) measurements were implemented with a 5 mV amplitude from 100 kHz to 0.01 Hz.

Results and discussion

Fig. 1a presents a preparation schematic of DTm@GC, illustrating the fabrication of ball-milled diatomite (DTm) composited with conductive carbon via hydrothermal and carbonization steps. The XRD patterns (Fig. 1b) demonstrate that the DT material mainly consists of two crystalline forms of SiO$_2$. The four diffraction peaks observed at 21.8°, 31.3°, 36°, and 42.4° are related to the (110), (102), (200) and (112) crystalline planes of cristobalite SiO$_2$ (JCPDS no. 27-0605),
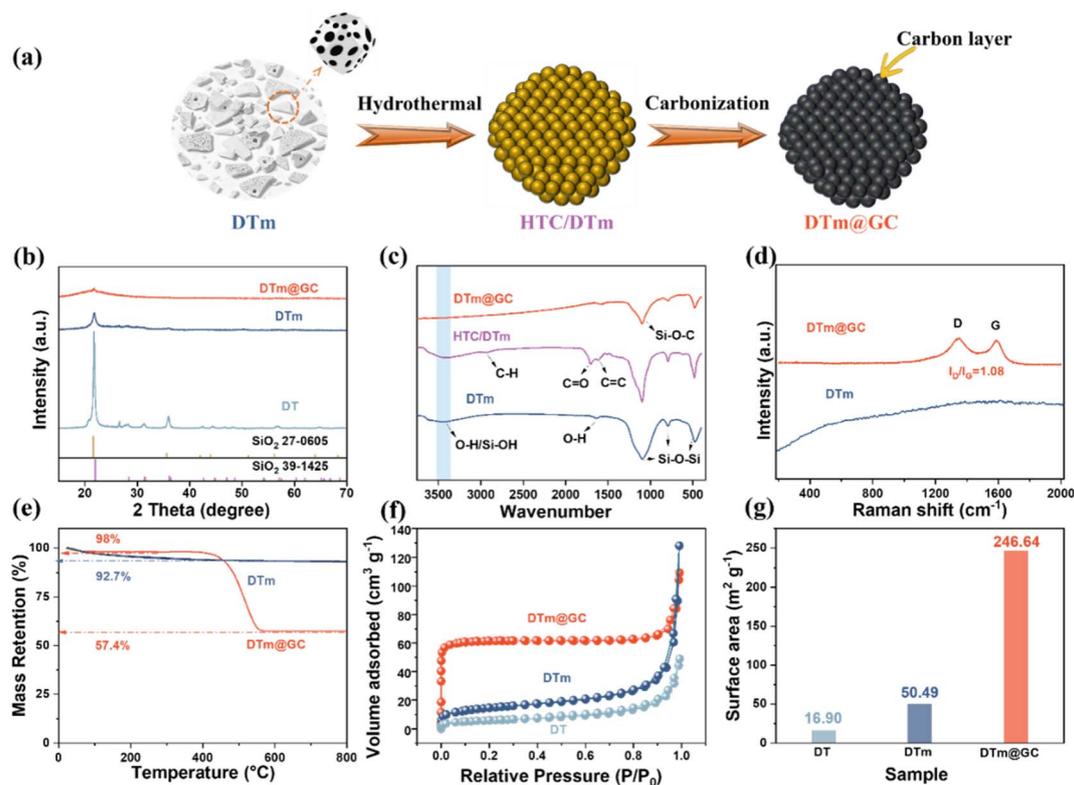

Fig. 1 (a) The synthesis schematic image of DTm@GC. (b) XRD patterns of DTm@GC, DTm and DT. (c) FTIR spectra of DTm@GC, HTC/DTm and DTm. (d) Raman spectra and (e) TG curves of DTm@GC and DTm. (f) Nitrogen adsorption–desorption curves and (g) surface areas of DT, DTm and DTm@GC.
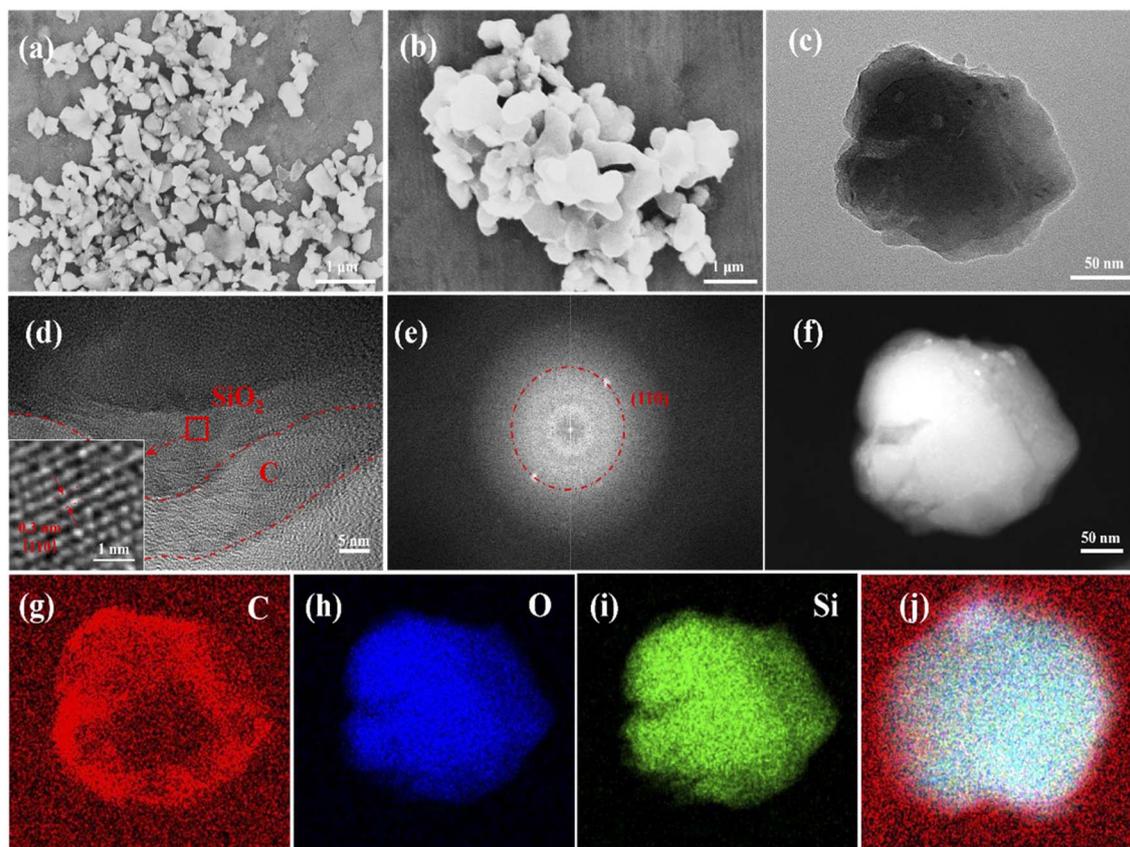
Fig. 2 (a and b) SEM images of DTm and DTm@GC. (c and d) Different resolution TEM images of DTm@GC. (e) Corresponding FFT image from (d). (f) Dark-field TEM image of DTm@GC, along with elemental mapping profiles of (g) C, (h) O, and (i) Si, and (j) the overlay image of DTm@GC.

respectively. The other crystalline peaks centred at 28.4°, 31.5° and 36.1° correspond to the (101), (111) and (102) lattice planes of α-quartz SiO_2 (JCPDS no. 39-1425), respectively.[27,28] The diffraction peak of DTm shows a broad width and reduced intensity after ball-milling treatment, indicating diminished crystalline size and increased structural disorder of DT. The diffraction pattern of DTm@GC shows a broad characteristic peak of amorphous carbon at around 22°, indicating the successful coating of the carbon layer on DTm.[29,30]

Fourier transform infrared (FTIR) spectroscopy was performed to track the evolution of chemical structure (Fig. 1c). All samples exhibit characteristic SiO_2 vibrations at 478 cm^{-1}, 795 cm^{-1}, and 1097 cm^{-1}, which correspond to Si–Si bending, Si–O–Si symmetric stretching, and Si–O–Si asymmetric stretching, respectively.[31,32] The weak peaks at 1637 cm^{-1} and 3420 cm^{-1} for DTm correlate with O–H vibrations of physically adsorbed water.[33] The FTIR spectrum of the intermediate product (HTC/DTm) after hydrothermal processing shows new vibrations of C–H, C=O and aromatic C=C, which are located at 2929 cm^{-1}, 1702 cm^{-1}, and 1616 cm^{-1}, respectively. This may be caused by the formation of carbonaceous species from glucose.[34,35] After the high temperature annealing process, DTm@GC exhibits a red shift of C=C vibration at 1577 cm^{-1}, along with disappearing peak signals of HTC. This observation is attributed to the carbonization treatment, which promotes

the aromatization of the carbon layer and ultimately forms a thermally stable structure dominated by aromatic carbon.[36,37] Due to the Si–O–C bonds located at around 990 cm^{-1} to 1190 cm^{-1}, it is difficult to distinguish them from the Si–O–Si bond at 1097 cm^{-1}.[38–40] Based on the attenuation of the adsorption peak intensity at 1100 cm^{-1}, it is inferred that a Si–O–C bond is generated after high temperature carbonization, owing to the combined glucose-driven carbon affecting the intensity of Si–O–Si bonds. This is similar to the evolution of Si–O–C bonds on C-doped amorphous SiO_2 modified by swift heavy ion irradiation.[41] It is beneficial to construct a stable chemical interface between the carbon layer and DTm materials, which can improve the electronic conductivity and structural robustness of DTm@GC.

Furthermore, the Raman spectra displayed in Fig. 1d are utilised to examine the structure of the carbon component on the surface of DTm@GC. Compared to DTm, the Raman spectrum of DTm@GC exhibits a clear D band (disorder-induced band, 1350.7 cm^{-1}) and G band (graphitic band, 1595.5 cm^{-1}), verifying the formation of a carbon coating on DTm@GC. The D band represents the breathing vibration mode of sp²-hybridized carbon in defective or disordered structures, while the G band stands for the in-plane vibration mode of sp²-bonded carbon pairs, reflecting a graphitized ordered structure and carbon lattice symmetry.[42,43] The intensity ratio of the D

band to G band (I_D/I_G) on the DTm@GC sample is measured as 1.08, higher than those of DTm@GC-2 and DTm@GC-6 (0.90 and 0.89, respectively, see Fig. S1), meaning a highly disordered and defective carbon layer on DTm@GC. Endowed with a disordered and defective structure, the carbon layer facilitates Li$^+$ diffusion, which in turn elevates the electrochemical properties of the DTm@GC anode.[44,45]

Thermogravimetric analysis (TG) curves of DTm and DTm@GC are shown in Fig. 1e, recorded in a heating temperature range up to 800 °C in an ambient atmosphere. A 6.3 wt% slight weight loss is observed in the TG curve of DTm, arising from the removal of adsorbed water on its surface. The mass retention rate of the DTm@GC sample is approximately 57.35 wt%, corresponding to diatomite-derived SiO$_2$ materials. The surface area and porous structure of the samples were examined by nitrogen adsorption–desorption analysis. As depicted in Fig. 1f and S2, all samples display type IV isotherms accompanied by H3-type hysteresis loops, a characteristic indicative of their mesoporous structure.[46] Notably, the specific surface area of DTm@GC reaches 246.64 m^2 g^{-1}, which is approximately 14 times that of DT (16.9 m^2 g^{-1}) and 5 times that of DTm (50.49 m^2 g^{-1}), as shown in Fig. 1g. This indicates that the synthesis procedure could construct a mass of ion diffusion channels on DTm@GC.

As displayed in the scanning electron microscopy (SEM) images of Fig. S3, the diameter of rounded DT is about 25 μm, which has a hierarchically porous structure. After ball milling, the size of DTm particles is significantly reduced to approximately 200 nm (Fig. 2a). DTm@GC exhibits larger particle size than DTm, due to the glucose-derived carbon uniformly covered on DTm nanoparticles (Fig. 2b). TEM (transmission electron microscopy) images of DTm@GC (Fig. 2c and d) reveal an amorphous structure of DTm with several crystalline silica domains, which is confirmed by the related fast Fourier transform (FFT) image in Fig. 2e. The crystalline silica domain exhibits a distinct lattice spacing of 0.3 nm (inset of Fig. 2d), which shows correspondence with the (110) plane of SiO$_2$ (JCPDS no. 39-1425) and validates the XRD analysis outcome. As demonstrated by the dark-field TEM image and elemental mapping images in Fig. 2f–j and S4, the silicon and oxygen in DTm@GC and HTC/DTm particles are uniformly distributed throughout particles. Their carbon signal is predominantly concentrated on the surface region of DTm@GC and HTC/DTm particles, meaning a well-defined continuous carbon layer on the surface.

Subsequently, X-ray photoelectron spectroscopy (XPS) characterization of the DTm, HTC/DTm, and DTm@GC materials revealed their chemical valence, with corresponding survey spectra displaying similar binding energy peaks of Si, O, and C elements (see Fig. 3a). The weak C 1s signal in DTm is a faint hint of carbon impurity. The fitting C 1s spectra of HTC/DTm and DTm@GC (Fig. 3b) show five binding energy peaks of C–C/C=C, C–O/Si–O–C, C=O, O–C=O, and π–π* satellites, mainly arising from glucose-derived hydrothermal carbon.[47,48] Notably, the intensity of the C–C/C=C peak in DTm@GC is significantly stronger than that of HTC/DTm, accompanied by
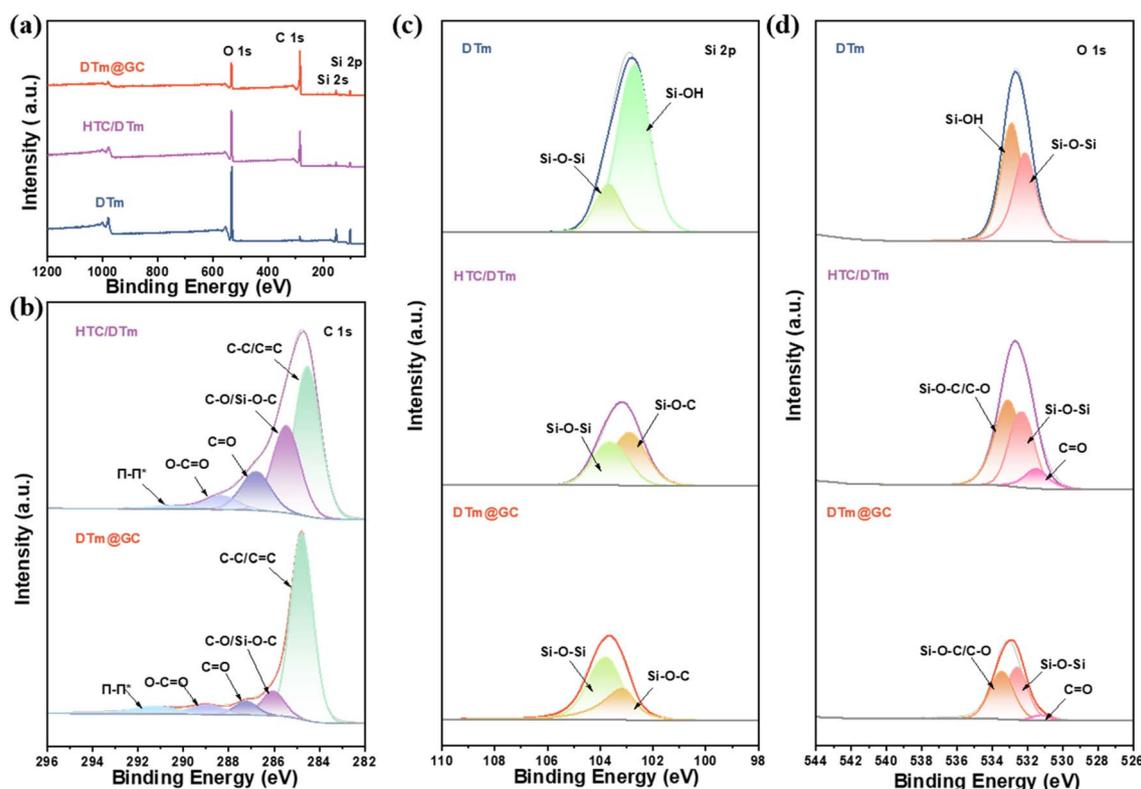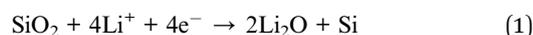

Fig. 3 (a) XPS survey spectra of DTm@GC, HTC/DTm, and DTm. (b–d) The corresponding spectra of C 1s, Si 2p, and O 1s.

a decrease in the intensities of C–O, C=O, and O–C=O bonds. This could be explained as the decomposition of HTC intermediates during high-temperature treatment.[49] Two peaks at 103.7 eV and 102.6 eV are obtained *via* deconvolution of the Si 2p spectrum in DTm (Fig. 3c), which belong to Si–O–Si and Si–OH components, respectively.[50] The component of Si–OH in DTm may be from the hydroxyl groups carried by DT transformed from diatoms. After hydrothermal treatment and carbonization, the Si–OH bond peak at 102.6 eV vanishes in both HTC/DTm and DTm@GC samples, while a new Si–O–C bond emerges at 103.1 eV in these two samples. The disappearance of the Si–OH bond is ascribed to the condensation reaction between surface Si–OH and hydrothermal glucose groups.[51] Meanwhile, the Si–O–C bonds that appear in HTC/DTm and DTm@GC are associated with the interfacial covalent transformation between the DTm surface and glucose-derived hydrothermal carbonization products under high-temperature conditions.[52] The two fitted peaks in the O 1s spectrum of DTm are assigned to Si–O–Si and Si–OH bonds, which are located at binding energies of 532.1 and 532.9 eV, respectively (Fig. 3d). Conversely, the O 1s spectrum of HTC/DTm exhibits three bonds of Si–O–C/C–O, Si–O–Si, and C=O, locating at binding energies of 533.1, 532.3, and 531.4 eV, respectively. The binding energy positions of Si–O–C/C–O and Si–O–Si in DTm@GC shift to 533.4 and 532.6 eV, which is primarily ascribed to the reduced oxygen content in the carbon layer following carbonization.[38,53] Thus, the anchored carbon layer could alter the electron density distribution of the Si–O bonds through covalent bonding, reducing the shielding effect on inner electrons and consequently increasing the binding energy of the Si 2p electrons.

The electrochemical properties of the LIB half-cell anodes are presented in Fig. 4. Firstly, as shown in Fig. 4a, DTm@GC exhibits the first discharge specific capacity of 1444.29 mA h g^{-1} at 0.1 A g^{-1} with initial coulombic efficiencies (ICE) of 51%. The substantial irreversible capacity loss of DTm@GC in the first cycle is primarily attributed to the high oxygen content of diatomite-derived silica consuming large quantities of Li$^+$ ions in the electrolyte, generating irreversible Li$_2$O and lithium silicate.[53] The first cycle performance of DTm@GC is much better than that of DTm, which may be owing to the construction of a Si–O–C bonded carbon network effectively enhancing the generation of reversible reduction intermediates. The reversible discharge specific capacity of DTm@GC reaches 781 mA h g^{-1} at 0.1 A g^{-1} after 100 consecutive cycles (Fig. 4a and b), indicating almost 100% capacity retention. By contrast, the DTm anode only achieves 176 mA h g^{-1} under similar testing conditions, which is considerably lower than that of the DTm@GC anode. Additionally, the DTm@GC anode retains a discharge specific capacity of 613.79 mA h g^{-1} over 200 consecutive cycles at 0.5 A g^{-1}, outperforming the DTm anode (100 mA h g^{-1}, Fig. S5). To investigate the influence of carbon layer thickness, reference samples with a thinner carbon layer (DTm@GC-2) and a thicker carbon layer (DTm@GC-6) are fabricated to examine the cell performances (Fig. S6). It is observed that DTm@GC-2 suffers from poor capacity retention (73.15%), while DTm@GC-6 shows a low specific capacity (493.19 mA h g^{-1}), indicating that an

optimal carbon layer can achieve a high capacity and ensure long-term cyclability. Furthermore, the advantage of the covalently bonded interface on DTm@GC can be verified by testing the electrochemical performance of DTm/GC, which is prepared by annealing the mixture of hydrothermal carbon products and DTm. When the half-cell LIBs are cycled at 0.5 A g^{-1}, the DTm/GC anode exhibits a specific capacity of just 173.68 mA h g^{-1} (Fig. S7), lower than that of DTm@GC (613.79 mA h g^{-1}). This may be caused by the incomplete carbon coating on the DTm/GC, resulting in discontinuous electronic conductivity and sluggish Li$^+$ migration. Moreover, the DTm@GC anode also exhibits an excellent capacity performance of 456.68 mA h g^{-1} at 1 A g^{-1} over 1000 cycles (Fig. S8), confirming a stable conductive network of covalently coated carbon material efficiently enhancing the capacity performance of silica. Regarding the rate performance (Fig. 4c–e), DTm@GC delivers reversible specific capacities of 769.83–316.19 mA h g^{-1} at current densities ranging from 0.1 to 2 A g^{-1}. Once the current density is set back to 0.1 A g^{-1}, the specific capacity of DTm@GC can recover to 781.79 mA h g^{-1}, reflecting the excellent rate performance and robust structure of DTm@GC. The average coulombic efficiencies of the DTm@GC anode at different current densities are higher than those of the DTm anode. This indicates that the covalently bonded Si–O–C interface between diatomite-derived SiO$_2$ and the conductive carbon network effectively promotes charge transfer and suppresses electrolyte decomposition, thereby enhancing the reversibility of lithium ion transportation. Furthermore, the cell performance of the DTm@GC anode is superior to those of reported SiO$_2$-based anodes in the literature, suggesting the large potential of DTm@GC for application in commercial products of LIBs (Fig. 4f).[25,52,54–60] In conclusion, the constructed carbon layer with the Si–O–C bond can efficiently enhance the stability of the carbon network, facilitate Li$^+$ diffusion, and alleviate the volume expansion of silica materials.

$$SiO_2 + 4Li^+ + 4e^- \rightarrow 2Li_2O + Si \tag{1}$$

$$2SiO_2 + 4Li^+ + 4e^- \rightarrow Li_4SiO_4 + Si \tag{2}$$

$$3SiO_2 + 4Li^+ + 4e^- \rightarrow 2Li_2SiO_3 + Si \tag{3}$$

$$5SiO_2 + 4Li^+ + 4e^- \rightarrow 2Li_2Si_2O_5 + Si \tag{4}$$

$$Si + xLi^+ + xe^- \rightarrow Li_xSi \tag{5}$$

The measured results of cyclic voltammetry (CV), galvanostatic intermittent titration technique (GITT), and electrochemical impedance spectroscopy (EIS) are used to elucidate the fundamental reason for the enhanced performance of DTm@GC. The CV curves of DTm@GC in Fig. 4g show that the initial cathodic peaks are located at 1.45 V, 0.90 V, and 0.58 V, along with a broad peak ranging from 0.01 to 0.4 V, corresponding to electrolyte decomposition, SEI film formation, silica lithiation, and an alloying reaction, respectively. Among these, SiO$_2$ lithiation involves irreversible reduction to Si, Li$_2$O, and lithium silicates (eqn (1)–(4)). The broad peak between
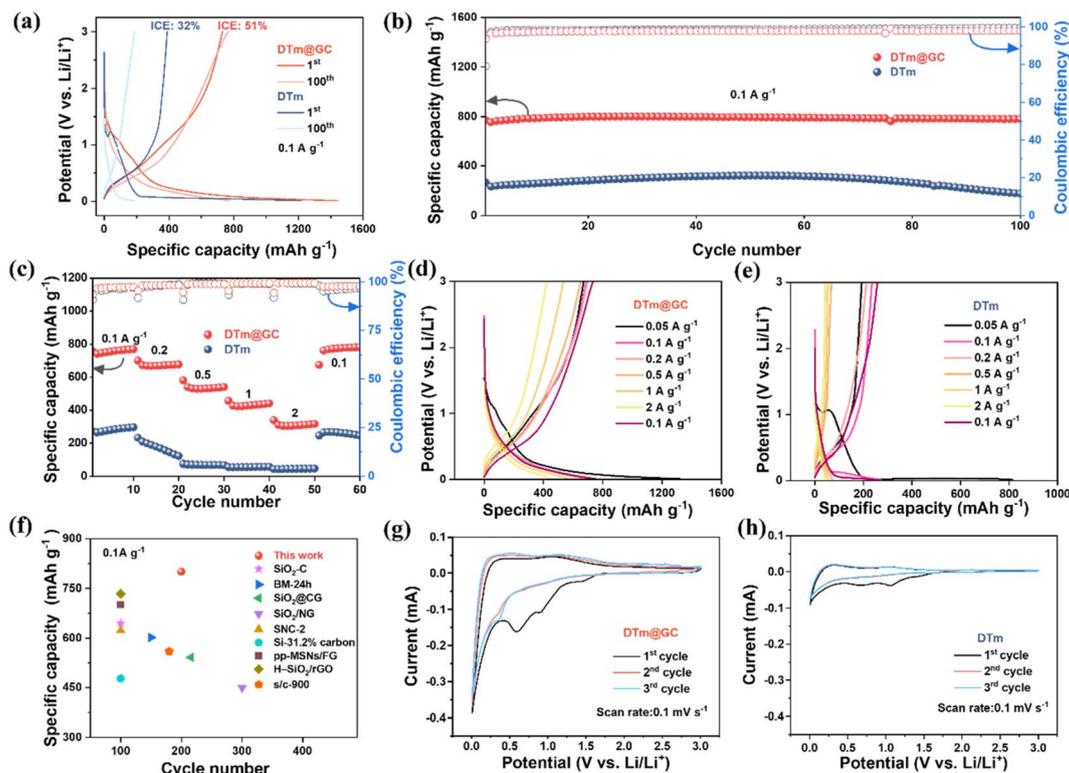
Fig. 4 (a) Charge–discharge curves of DTm@GC and DTm anodes at the first cycle and the 100th cycle at 0.1 A g^{-1}. (b) Cycling stability of DTm@GC and DTm anodes at 0.1 A g^{-1} after being activated at 0.05 A g^{-1} for 3 cycles. (c) Rate capacity curves of the DTm@GC and DTm anodes. (d and e) Charge–discharge curves of DTm@GC and DTm anodes at current densities ranging from 0.1 A g^{-1} to 2 A g^{-1} after being activated at 0.05 A g^{-1} for 3 cycles. (f) Comparison of the DTm@GC anode developed in this work with other SiO$_2$-based anodes for LIBs. (g and h) CV curves of DTm@GC and DTm anodes.

0.01 V and 0.4 V indicates generation of Li$_x$Si through an alloying reaction (eqn (5)). In the anodic segment of the CV curve, the oxidative peaks at 0.5 V and 1.0 V are respectively related to processes of dealloying and lithium silicate oxidation.[61] The reduction peak detected at 0.35 V in the CV curves is ascribed to the sustained intercalation of Li$^+$ into the silicon matrix, forming a lithium–silicon (Li$_x$Si) alloy. This phenomenon demonstrates that a stable Li$^+$ insertion/extraction process is established in the materials. The CV curves of the DTm electrode in Fig. 4h exhibit the same reduction peaks with DTm@GC, indicating the similar electrochemical behaviour of the two samples.[55] But the CV curves of DTm@GC exhibit larger peak currents than those of DTm, owing to its higher conductivity and better structural stability. This comparative analysis has clearly demonstrated that DTm@GC can achieve superior electrochemical activity and reversibility because the coupling carbon layer has modified the electronic conductivity and mitigated the volume variation of silica.

To explore the Li$^+$ storage mechanism, the CV curves of DTm@GC, DTm, and DTm/GC scanned at various rates are illustrated in Fig. 5a and b and S9, respectively. The equation provided below can be utilized to establish a correlation between measured current (i) and scan rate (v):[62]

$$i = av^b \qquad (6)$$

which is linearized as:

$$\log(i) = b\log(v) + \log(a) \qquad (7)$$

where a and b, respectively, represent a constant and a slope of the log(i) vs. log(v) curve. When the b value is calculated to be 0.5, its reaction process is considered to be a diffusion-controlled step. By contrast, the process is controlled by a pseudocapacitive contribution as the b value nears 1. The anodic b value of DTm@GC in Fig. 5c is 0.83, which is lower than those of DTm/GC (0.92, Fig. S10) and DTm (0.98, Fig. S11). The b value of DTm@GC locates between 0.5 and 1, indicating that the lithium ion behaviour in DTm@GC is synchronously controlled by pseudocapacitive and diffusion processes. The Li$^+$ storage processes of DTm/GC and DTm are mainly dominated by the pseudocapacitive contribution, as their b values are close to 1. Furthermore, the Li$^+$ diffusion coefficients and capacitive contributions of samples at different scan rates are calculated using the following equation:[63]

$$i = k_1 v + k_2 v^{1/2} \qquad (8)$$

where $k_1 v$ relates to pseudocapacitive contributions, while $k_2 v^{1/2}$ is associated with the diffusion-controlled region.

As displayed in Fig. 5d and e, the calculated capacitive contribution of DTm@GC increases from 48% to 81% as the
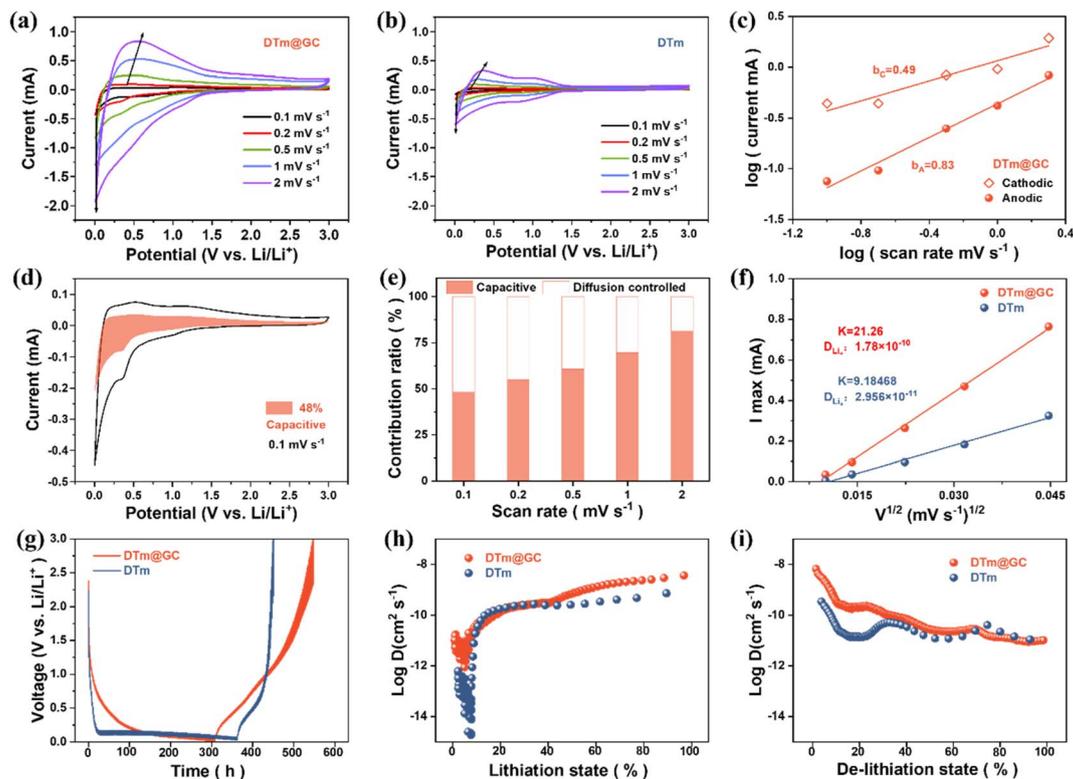
Fig. 5 CV curves at various scan rates of (a) DTm@GC and (b) DTm. (c) *b* values of DTm@GC at different peak currents after linear fitting. Pseudocapacitive contribution of DTm@GC at (d) 0.1 mV s^{-1} and (e) different scan rates. (f) Linear fitting between peak current and scan rates for DTm@GC and DTm. (g–i) GITT voltage profiles and Li$^+$ diffusion coefficients of DTm@GC and DTm electrodes.

scan rate rises from 0.1 to 2 mV s^{-1}. The diffusion contribution shows a gradually decreasing trend with increasing scan rate, which is in good agreement with the typical kinetic behaviour of battery-type electrodes. Specifically, at higher scan rates, Li$^+$ ions can only react on the surface or near-surface regions of the electrode, and the charge storage process is gradually dominated by the pseudocapacitive contribution, leading to an elevated pseudocapacitance ratio and a correspondingly reduced diffusion contribution. The pseudocapacitive contributions of DTm@GC are lower than those of DTm/GC (Fig. S12) at the same scan rates, indicating the co-operation of pseudocapacitive and diffusion processes in DTm@GC. Furthermore, the fitting results in Fig. 5f and S13 reveal that DTm@GC exhibits a Li$^+$ diffusion coefficient of 1.78×10^{-10} cm^2 s^{-1}, superior to that of DTm (2.956×10^{-11} cm^2 s^{-1}) and DTm/GC (8.444×10^{-11} cm^2 s^{-1}). This result suggests the highly efficient electron and ion transport in DTm@GC, attributed to the covalently anchored carbon layer. To verify the electrochemical activity of electrodes, GITT plots in Fig. 5g are collected at 0.01–3.0 V under a 0.05 C current pulse (600 s) and subsequent 3600 s relaxation. The lithium-ion diffusion coefficient (D_{Li^+}) is derived from the formula provided below:[64]

$$D_{Li^+} = \frac{4}{\pi\tau}\left(\frac{m_B V_M}{M_B S}\right)^2 \left(\frac{\Delta E_S}{\Delta E_\tau}\right)^2 \quad \left(\tau \ll \frac{L^2}{D}\right) \quad (9)$$

where τ is the duration of the current pulse, m_B denotes the active material mass, V_M corresponds to the molar volume, M_B

stands for the molar mass, S stands for the electrode surface area, ΔE_s refers to the voltage variation during the pulse, and ΔE_τ represents the steady-state voltage variation. As shown in Fig. 5h and i, the DTm@GC electrode exhibits a higher Li$^+$ diffusion coefficient than the DTm electrode during both charge and discharge processes, confirming that the large surface area and high conductivity of the DTm@GC anode are beneficial for enhancing the electrochemical activity with rapid ion diffusion.

Additionally, *in situ* EIS collected during the initial discharge/charge cycle are used to elucidate the electrochemical behaviour and structural variation of the samples (Fig. 6a and b).[65] As shown in the equivalent circuit diagram in the insets of Fig. 6a and b, R_s represents the ohmic resistance, the semicircle plot relates to the charge transfer resistance (R_{ct}), and the straight line corresponds to Li$^+$ diffusion resistance (W_s), respectively. At the open-circuit potential, the smaller R_{ct} (195.76 Ω) of DTm@GC than DTm (547.44 Ω) indicates the significantly enhanced electronic conductivity arising from the covalently anchored carbon layer (Table S1). As the voltage decreases, cell impedance becomes smaller and smaller due to the generation of an SEI, lithium silicates, Li$_2$O, and Li$_x$Si alloy. The R_{ct} values of DTm@GC are still smaller than those of DTm during the charging process (0.01 to 3 V, Table S1), suggesting superior conductivity and fast Li$^+$ migration of DTm@GC. The low R_{ct} values of DTm@GC in *in situ* EIS spectra at different cycles (Fig. S14) have also confirmed the fast electrode kinetics
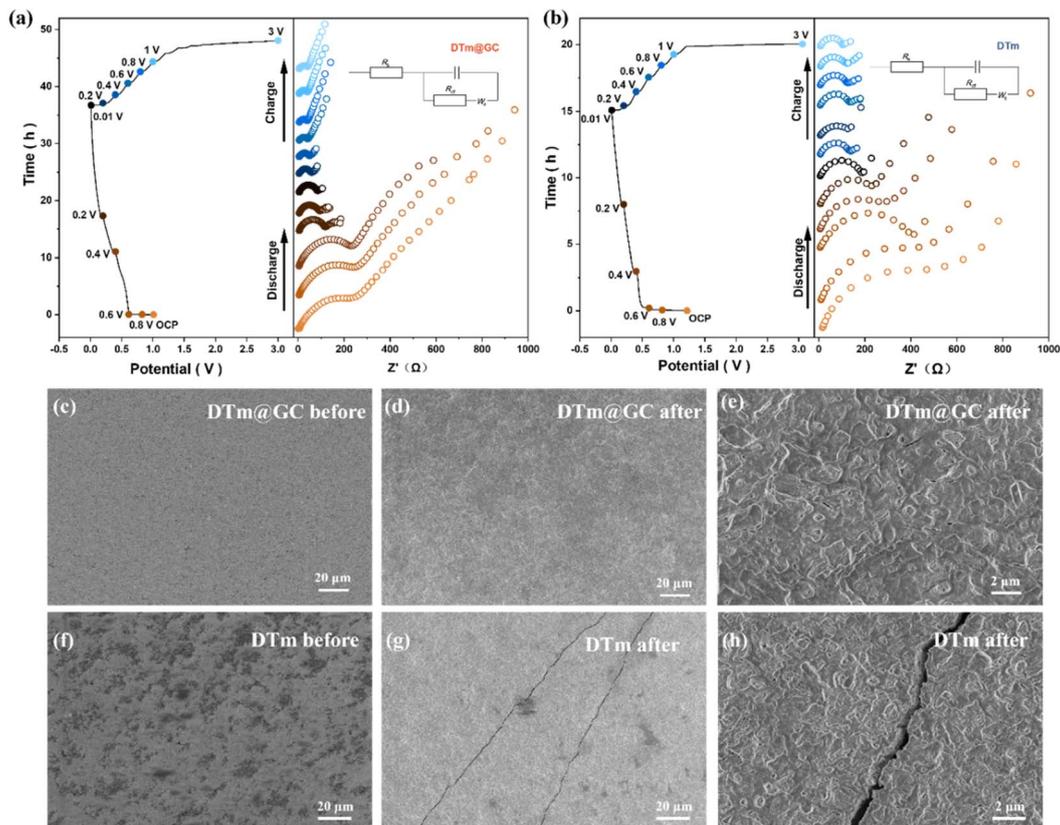
Fig. 6   (a and b) The *in situ* EIS spectra recorded during the initial discharge/charge process of DTm@GC and DTm anodes (inset: equivalent circuit diagram). SEM images of (c–e) the DTm@GC anode and (f–h) DTm anode before and after 1000 cycles at 1 A g^{-1}.

of DTm@GC during charge/discharge processes, due to a dense and stable SEI constructed on the anode surface. Additionally, the morphologies of the anodes are characterized before and after 1000 cycles at 1 A g^{-1} to explore the volume variation of electrodes. As illustrated in Fig. 6c–e, the DTm@GC anode after 1000 cycles at 1 A g^{-1} retains a uniform surface without cracks, demonstrating that the covalently coated carbon layer can suppress particle pulverization and volumetric strain during lithiation/de-lithiation. In contrast, the surface of the DTm electrode after long-term cycling shows many cracks, which reflects substantial volume expansion of DTm throughout the cycling process (Fig. 6f–h). Therefore, the covalently coated carbon structure can optimize the electronic conductivity and volume strain of silica particles, thereby significantly improving the cell performance of the DTm@GC anode.

Finally, the electrochemical measurements of a full cell composed of the DTm@GC anode and lithium iron phosphate (LFP) cathode (denoted as DTm@GC//LFP) are shown in Fig. S15. The CV curves of the DTm@GC//LFP full cell in Fig. S15a exhibit a distinct redox peak in a voltage range of 2.5–3.8 V, corresponding to lithium ion intercalation/deintercalation reactions between DTm@GC and LFP electrodes. Fig. S15b shows that the voltage plateaus of the charge/discharge curves are related to the oxidative and reductive peaks in the CV profiles, demonstrating stable electrochemical reaction behaviour of the DTm@GC//LFP full cell. As depicted in

Fig. S15b and c, the DTm@GC//LFP full cell delivers a discharge specific capacity of approximately 112.45 mA h g^{-1} at 0.5 C. The capacity retention of the DTm@GC//LFP full cell is 59% after 200 cycles. The capacity fading of the DTm@GC//LFP full cell may be caused by the limited lithium ion resources provided by the electrolyte and LFP cathode. The inevitable volume strain of DTm@GC would slowly consume the limited lithium resources and cause irreversible lithium loss, resulting in the decline of cell performance. Furthermore, a 5 V light bulb (Fig. S15d) can be lit up by a circuit composed of two series-connected DTm@GC//LFP button cells, holding great promise for DTm@GC in numerous practical applications.

Conclusions

In summary, DTm@GC with a continuous carbon network was successfully fabricated as an efficient anode for LIBs. This DTm@GC anode shows outstanding electrochemical performances, retaining a discharge specific capacity of 781 mA h g^{-1} after 100 cycles at 0.1 A g^{-1} without capacity degradation, making it superior to pure DTm. Moreover, the DTm@GC anode retains an outstanding capacity performance of 456.68 mA h g^{-1} at 1 A g^{-1} after a stability test of 1000 cycles. This enhanced capacity is attributed to the dense and strong Si–O–C covalent bonds between the carbon coating and silica matrix, which play crucial roles in facilitating efficient electron

transfer and mitigating the volume variation of SiO_2, thereby optimizing the electrode activity and structural integrity of the DTm@GC. These results demonstrate that DTm@GC represents a viable anode material for high-energy-density LIBs, providing new insights into development of SiO_2-based anodes for sustainable energy storage.

Author contributions

Qiaofu Zheng: methodology design, experimental investigations, validation work, data curation and analysis, original manuscript drafting, and paper review and revision. Licheng Wei: experimental protocol formulation, material performance evaluation, experimental feasibility analysis, initial draft composition, and manuscript review and refinement. Lifeng Zhou: fabrication and characterization of anode materials. Guannan Peng: preparation and property characterization of anode materials. Dalei Sun: experimental feasibility assessment. Yimin Chao: research framework conceptualization, technical methodology development, funding acquisition coordination, research resource allocation, experimental outcome verification, and manuscript drafting, reviewing and finalizing.

Conflicts of interest

All authors confirm that they have no potential conflict of interest.

Data availability

All original research data and contributions of this study are contained within the published paper and supporting information (SI). Further questions can be addressed to the corresponding authors for clarification. Supplementary information is available. See DOI: https://doi.org/10.1039/d6su00026f.

Acknowledgements

Notes and references

1 B. Bose, A. Garg, B. K. Panigrahi and J. Kim, *J. Energy Storage*, 2022, **55**, 105507.

2 Y. Tang, Y. Zhang, W. Li, B. Ma and X. Chen, *Chem. Soc. Rev.*, 2015, **44**, 5926–5940.

3 X. Y. Liu, Q. N. Zhu, A. Jiang, J. X. Yue, D. D. Yu, S. C. Wang, S. Dong, J. H. Zhao, W. H. Wang, S. Lyu, J. W. Wang, L. T. Shi, Y. H. Guo, W. L. Song, Y. J. Liu, J. Nai, R. H. Wang and H. Wang, *Adv. Funct. Mater.*, 2025, e21637, DOI: 10.1002/adfm.202521637.

4 Q. N. Zhu, L. W. Cheng, X. Y. Sun, J. Q. Huang, J. W. Wang, S. Dong, M. Kurbanov, L. Guo and H. Wang, *Adv. Mater.*, 2025, **37**, 2419041.

5 S. Javadian, E. Bayat, Z. Parviz, N. Dalir and H. Gharibi, *New J. Chem.*, 2021, **45**, 11737–11751.

6 H. Ruan, S. Guo, L. Zhang, Y. Liu, L. Li, Y. Huang, S. Gao and Y. Tian, *Ceram. Int.*, 2022, **48**, 17510–17517.

7 G. F. I. Toki, M. K. Hossain, W. U. Rehman, R. Z. A. Manj, L. Wang and J. Yang, *Ind. Chem. Mater.*, 2024, **2**, 226–269.

8 K. Cheng, S. Tu, B. Zhang, W. Wang, X. Wang, Y. Tan, X. Chen, C. Li, C. Li, L. Wang and Y. Sun, *Energy Environ. Sci.*, 2024, **17**, 2631–2641.

9 J. D. McBrayer, M.-T. F. Rodrigues, M. C. Schulze, D. P. Abraham, C. A. Apblett, I. Bloom, G. M. Carroll, A. M. Colclasure, C. Fang, K. L. Harrison, G. Liu, S. D. Minteer, N. R. Neale, G. M. Veith, C. S. Johnson, J. T. Vaughey, A. K. Burrell and B. Cunningham, *Nat. Energy*, 2021, **6**, 866–872.

10 S. Park, S. Y. Jeong, T. K. Lee, M. W. Park, H. Y. Lim, J. Sung, J. Cho, S. K. Kwak, S. Y. Hong and N. S. Choi, *Nat. Commun.*, 2021, **12**, 838.

11 J. C. Yang, S. C. Wang, S. Y. Song, D. An, X. W. Yu, Q. N. Zhu, D. D. Yu, J. W. Wang, S. Dong, J. Nai, J. Yang, Z. H. Ma, M. Kurbanov, B. Gao and H. Wang, *Adv. Mater.*, 2025, **37**, 2501807.

12 M. Zhu, Y. Shen, L. Chang, D. Yin, Y. Cheng and L. Wang, *Nanoscale*, 2020, **12**, 13442–13449.

13 J. Wang, D.-H. Liu, Y.-Y. Wang, B.-H. Hou, J.-P. Zhang, R.-S. Wang and X.-L. Wu, *J. Power Sources*, 2016, **307**, 738–745.

14 K. Wang, X. Zhu, Y. Hu, S. Qiu, L. Gu, C. Wang and P. Zuo, *Carbon*, 2020, **167**, 835–842.

15 S. Ko, X. Han, T. Shimada, N. Takenaka, Y. Yamada and A. Yamada, *Nat. Sustainability*, 2023, **6**, 1705–1714.

16 M. Jiao, Y. Wang, C. Ye, C. Wang, W. Zhang and C. Liang, *J. Alloys Compd.*, 2020, **842**, 155774.

17 D. Wang, D. Zhang, Y. Dong, X. Lin, R. Liu, A. Li, X. Chen and H. Song, *ACS Appl. Energy Mater.*, 2021, **4**, 6146–6153.

18 J. Zou, S. Yuan, Y. Huang, X. Du, C. Chen and J. Wang, *Nanotechnology*, 2023, **34**, 455404.

19 J. Wu, Q. Dong, Q. Zhang, Y. Xu, X. Zeng, Y. Yuan and J. Lu, *Adv. Mater.*, 2024, **36**, e2405751.

20 J.-Y. Kim, D. T. Nguyen, J.-S. Kang and S.-W. Song, *J. Alloys Compd.*, 2015, **633**, 92–96.

21 F. Lepoivre, D. Larcher and J.-M. Tarascon, *J. Electrochem. Soc.*, 2016, **163**, A2791–A2796.

22 X. Ma, Z. Wei, H. Han, X. Wang, K. Cui and L. Yang, *Chem. Eng. J.*, 2017, **323**, 252–259.

23 T. Ludwig, M. Je, H. Choi, T. Fischer, S. Roitsch, R. Müller, R. S. Mane, K. H. Kim and S. Mathur, *Nano Energy*, 2020, **78**, 105286.

24 H. Dunya, M. Ashuri, Z. Yue, K. Kucuk, Y. Lin, D. Alramahi, C. U. Segre and B. K. Mandal, *J. Phys. Chem. Solids*, 2021, **149**, 109791.

25 D. Zhang, Q. Shu, Y. Zhang, H. Nui, X. Hu, P. Guan and X. Wang, *J. Appl. Electrochem.*, 2024, **55**, 35–51.

26 X. Liu, Y. Chen, H. Liu and Z.-Q. Liu, *J. Mater. Sci. Technol.*, 2017, **33**, 239–245.

27 S. Sembiring and W. Simanjuntak, *Makara J. Sci.*, 2012, **16**, 1.

28 O. Şan and C. Özgür, *J. Eur. Ceram. Soc.*, 2009, **29**, 2945–2949.

29 W. Long, B. Fang, A. Ignaszak, Z. Wu, Y. J. Wang and D. Wilkinson, *Chem. Soc. Rev.*, 2017, **46**, 7176–7190.

30 M. V. Blanco, V. Renman, J. Zhu, F. Vullum-Bruer and A. M. Svensson, *J. Solid State Electrochem.*, 2021, **25**, 1339–1351.

31 S. A. El-Khodary, G. Subburam, B.-B. Zou, J. Wang, J.-X. Qiu, X.-H. Liu, D. H. L. Ng, S. Wang and J.-B. Lian, *Rare Met.*, 2021, **41**, 368–377.

32 Y. Zheng, Z. Liu, B. Liu, S. Wang and C. Xiong, *Energy*, 2021, **217**, 2306351.

33 X. Huang, Y. Ding, K. Li, X. Guo, Y. Zhu, Y. Zhang and Z. Bao, *J. Power Sources*, 2021, **496**, 229833.

34 M. Barańska, K. Chruszcz, B. Boduszek and L. M. Proniewicz, *Vib. Spectrosc.*, 2003, **31**, 295–311.

35 D. Cheng, Y. Wen, X. An, X. Zhu and Y. Ni, *Carbohydr. Polym.*, 2016, **151**, 326–334.

36 X. Zhou, Y. Liu, C. Du, Y. Ren, T. Mu, P. Zuo, G. Yin, Y. Ma, X. Cheng and Y. Gao, *J. Power Sources*, 2018, **381**, 156–163.

37 S. Wang, S. Zhao, B. B. Uzoejinwa, A. Zheng, Q. Wang, J. Huang and A. E.-F. Abomohra, *Energy Convers. Manage.*, 2020, **222**, 113253.

38 S. Yang, Y. Tang, Z. Yang, S. Yang, B. Li, W. Peng, B. Peng, G. Wang, J. Liang, J. Ji and F. Yu, *Green Chem.*, 2025, **27**, 1997–2007.

39 S. Yang, Y. Tang, Z. Yang, B. Li, G. Wang, J. Liang, L. Zhang and F. Yu, *Carbon*, 2025, **233**, 119881.

40 T. Oh and C. K. Choi, *J. Kor. Phys. Soc.*, 2010, **56**, 1150–1155.

41 Z. G. Wang, Z. M. Zhao, A. Benyagoub, M. Toulemonde, F. Levesque, Y. Song, Y. F. Jin, Y. M. Sun, C. B. Liu, H. Zang and K. F. Wei, *Nucl. Instrum. Methods Phys. Res. Sect. B Beam Interact. Mater. Atoms*, 2007, **256**, 288–292.

42 L. Shi, Y. Li, Y. Xing, R. Lin, G. Cheng, J. Ding and K. H. Lam, *Electrochim. Acta*, 2021, **390**, 138841.

43 Y. Wang, C. Xu, J. Fu, S. Che, G. Ma, K. Chen, J. Yang, S. Liu, G. Cheng, D. Zhang, Y. Huang, W. Gao, Y. Cui and Y. Li, *Chem. Eng. J.*, 2025, **510**, 161895.

44 S. Urbonaite, L. Hälldahl and G. Svensson, *Carbon*, 2008, **46**, 1942–1947.

45 S. Javadian, A. Zeinodiny, N. Dalir, H. Gharibi and S. M. J. Ghavam, *Mater. Chem. Phys.*, 2023, **298**, 127447.

46 X. Song, X. Zhou and X. Lv, *J. Asian Earth Sci.*, 2023, **247**, 105595.

47 H. Xiong, L. Ding, B. Xu, B. Liang and F. Yuan, *IEEE Sens. J.*, 2021, **21**, 10392–10399.

48 S. A. El-Khodary, A. E. Abomohra, G. M. El-Enany, A. A. Aboalhassan, D. H. L. Ng, S. Wang and J. Lian, *Ultrason. Sonochem.*, 2019, **58**, 104617.

49 Y. Lin, H. Xu, Y. Gao and X. Zhang, *Biomass Convers. Biorefinery*, 2021, **13**, 3785–3796.

50 Y. Lin, J. Jiang, Y. Zhang, X. He, J. Ren, P. He, C. Pang, C. Xiao, D. Yang and N. Du, *Chem. Mater.*, 2020, **32**, 6365–6373.

51 Y. X. Chen, H. C. Liu, W. Q. Xie, Z. Shen, J. L. Xia, Z. Y. Nie and J. P. Xie, *Small*, 2023, **19**, e2300707.

52 J. Liang, S. Yang, L. Ye, X. Li, X. Yang, S. Chen and P. Liu, *J. Mater. Sci.: Mater. Electron.*, 2021, **32**, 28119–28128.

53 W. Shen, C. Zhang, M. Alomar, Z. Du, Z. Yang, J. Wang, G. Xu, J. Zhang, J. Lv and X. Lu, *Nano Res.*, 2023, **17**, 1217–1224.

54 S. Ali, S. Jaffer, I. Maitlo, F. K. Shehzad, Q. Wang, S. Ali, M. Y. Akram, Y. He and J. Nie, *J. Alloys Compd.*, 2020, **812**, 152127.

55 C. Liang, L. Zhou, C. Zhou, H. Huang, S. Liang, Y. Xia, Y. Gan, X. Tao, J. Zhang and W. Zhang, *Mater. Res. Bull.*, 2017, **96**, 347–353.

56 L.-h. Yin, M.-b. Wu, Y.-p. Li, G.-l. Wu, Y.-k. Wang and Y. Wang, *N. Carbon Mater.*, 2017, **32**, 311–318.

57 X. Guo, W. Li, P. Geng, Q. Zhang, H. Pang and Q. Xu, *J. Colloid Interface Sci.*, 2022, **606**, 784–792.

58 D. Jia, K. Wang and J. Huang, *Chem. Eng. J.*, 2017, **317**, 673–686.

59 H. H. Li, L. L. Zhang, C. Y. Fan, K. Wang, X. L. Wu, H. Z. Sun and J. P. Zhang, *Phys. Chem. Chem. Phys.*, 2015, **17**, 22893–22899.

60 H. Chu, Q. Wu and J. Huang, *Colloids Surf., A Physicochem. Eng. Asp.*, 2018, **558**, 495–503.

61 Y. Qi, G. Wang, S. Li, T. Liu, J. Qiu and H. Li, *Chem. Eng. J.*, 2020, **397**, 125380.

62 S. Javadian, M. Moslemi, H. Gharibi, Z. Parviz, N. Dalir and A. Zeinodiny, *J. Power Sources*, 2025, **629**, 235974.

63 Z. Yang, C. Wu, S. Li, L. Qiu, Z. Yang, Y. Zhong, B. Zhong, Y. Song, G. Wang, Y. Liu, Z. Wu and X. Guo, *Adv. Funct. Mater.*, 2021, **32**, 2107897.

64 M. Bai, X. Tang, M. Zhang, H. Wang, Z. Wang, A. Shao and Y. Ma, *Nat. Commun.*, 2024, **15**, 5375.

65 H.-W. Yang, W. S. Kang and S.-J. Kim, *Electrochim. Acta*, 2022, **412**, 140107.